Three-Dimensional Scattering by Two-Dimensional Topographies

by H. A. Pedersen, F. J. Sánchez-Sesma, and M. Campillo

Abstract Three-dimensional seismic responses of two-dimensional topographies are studied by means of the indirect boundary element method (IBEM). The IBEM yields, in the presented form, very accurate results and has the advantage of low computational cost. In IBEM, diffracted waves are constructed in terms of single-layer boundary sources. The appropriate Green's functions used are those of a harmonic point force moving along the axis of the topography in a full space. Obtained results are compared against those published by other authors. Examples of simulations are presented for different geometries, for different types of incident wave fields, and, in particular, for different arrival angles to the topography to quantitatively study three-dimensional effects of the scattering. The accuracy of the results makes it possible to analyze them in both the time and frequency domains. Frequency-space representations allow identification of diffraction and interference patterns in the seismic response of the topography. Synthetic seismograms are obtained by Fourier analysis. Using time-space domain representations, the nature of each of the scattered waves are identified in terms of, for example, creeping waves and reflected compressional waves.

Introduction

Surface topography has been reported to produce significant site effects (e.g., Davis and West, 1973; Griffiths and Bollinger, 1979; Bard and Tucker, 1985). These effects take the form of a relative amplification of seismic signals recorded at the top of a mountain with respect to a reference station located at the base of the mountain. The relative amplification can be significant over a large frequency interval. Knowledge of these effects is important for the prediction of ground movement close to topographic features.

Two-dimensional topographic effects on wave fields have been numerically modeled by a number of authors. Analytical solutions have been found for simple geometries (Trifunac, 1973; Lee and Cao, 1989; Todorovska and Lee, 1990, 1991). Bouchon (1973), Bard (1982), and Geli *et al.* (1988) have used techniques based on the method proposed by Aki and Larner (1970) to model topographic effects. A large number of simulations have been performed with techniques based on representation theorems. These methods include the direct boundary element method (BEM) (Wong and Jennings, 1975; Zhang and Chopra, 1991), the indirect boundary element method (IBEM) (Sánchez-Sesma and Rosenblueth, 1979; Wong, 1982; Luco *et al.*, 1990; Sánchez-Sesma and Campillo, 1991, 1993), and combinations of integral representations with discrete wavenumber expansions of Green's functions (Bouchon, 1985; Kawase, 1988; Pei and Pa-

pageorgiou, 1993a). While BEM directly finds the unknown tractions and displacements, IBEM searches a force distribution for which the radiated field satisfies the boundary conditions. Displacements are obtained by superposition of the radiation from these sources. A more detailed discussion of the use of these methods in site effect simulations can be found in Sánchez-Sesma and Campillo (1993).

While theoretical models predict significant scattering by topographies, they have not yet quantitatively explained observations (e.g., Bard and Tucker, 1985; Geli *et al.*, 1988). Some observations seem to show both higher and more broadband amplification than predicted by numerical simulations. To evaluate whether topographic effects alone can account for the observed amplifications, it is necessary to extend the numerical simulation to geologically more realistic models, taking into account the three-dimensional character of real topographies and the presence in nature of all types of incident wave fields.

Different attempts have been made to extend the simulation of scattering by two-dimensional structures from pure two-dimensional scattering (incident wave field perpendicular to the structure) to three-dimensional scattering (incident wave field with an arbitrary arrival angle to the structure). In particular, to study the diffraction by a canyon, Luco *et al.* (1990) use IBEM and locate

sources off the surface of the canyon to displace singularities in the Green's functions from the surface. In this approach, sources must be carefully located to avoid numerical problems and the location off the surface leads to an approximate solution. Pei and Papageorgiou (1993a) simulate the scattered wave field across a canyon by using half-space Green's functions to solve the boundary integral equation on the surface itself. While more accurate, the latter method has a high computational cost as a result of the calculation of half-space Green's functions. Three-dimensional scattering by two-dimensional structures has also been treated in the case of alluvial valleys (Khair *et al.*, 1989; Khair *et al.*, 1991; Liu *et al.*, 1991; Pei and Papageorgiou, 1993b).

In this article we present a method to simulate three-dimensional scattering by ridge and canyon structures of arbitrary shapes. The IBEM, with full space Green's functions, is used to create the scattered wave field. By using compact expressions of Green's functions appropriate to the problem, highly accurate results are produced for a low computational cost. The method, therefore, makes it possible to perform a large number of simulations for the study of how different parameters influence the scattering and for the study of three-dimensional effects due to the obliquely incident waves. It is possible, in particular, to quantitatively model observed site effects on topographies because the arrival angle of the incident waves on the structure can be taken into account.

The article is organized as follows: first, a brief introduction is given to IBEM, and then compact expressions for Green's functions are derived for use in the simulations. The theoretical part is concluded by a discussion of the implementation of the method. Results from applying the method are compared against those from other approaches, and finally, examples are presented of simulations performed for simple geometries.

Integral Representation of Elastic Wave Fields

The IBEM is based on an integral representation of wave fields. Neglecting body forces, the displacement field in a domain V with boundary S occupied by an elastic material can be written (see Sánchez-Sesma and Campillo, 1991)

$$u_i(\mathbf{x}) = \int_s \psi_j(\boldsymbol{\zeta}) \, G_{ij}(\mathbf{x}, \boldsymbol{\zeta}) dS_\zeta, \qquad (1)$$

where $u_i(x)$ is the *i*th component of displacement at $\mathbf{x}$. The term $G_{ij}(\mathbf{x}, \boldsymbol{\zeta})$ is the Green's function; i.e., the displacement in direction i at $\mathbf{x}$ due to a point force in direction j applied at the point $\boldsymbol{\zeta}$; $\psi_j(\boldsymbol{\zeta})$ is the force density in direction j at $\boldsymbol{\zeta}$. The term $\psi_j(\boldsymbol{\zeta})dS_\zeta$ is therefore a force

distribution on S. The integration is performed over the space variable $\boldsymbol{\zeta}$.

Equation (1) shows that if G_{ij} is known, one simply needs to find the force density ψ_j on the surface S to calculate the displacement at any point in V. Furthermore, the displacement field is continuous across S if ψ_j is continuous on S (Kupradze, 1963). When displacements u_i are known, it is possible to calculate stresses and tractions by applying Hooke's law. Special care must be taken at boundary singularities. The contribution of the singularity to the traction equals half the surface force applied, assuming a smooth boundary (e.g., Kupradze, 1963),

$$t_i(\mathbf{x}) = c\psi_i(\mathbf{x}) + \int_s \psi_j(\boldsymbol{\zeta})T_{ij}(\mathbf{x}, \boldsymbol{\zeta})dS_\zeta, \qquad (2)$$

where $t_i(\mathbf{x})$ is the *i*th component of traction at $\mathbf{x}$; c equals 0 if $\mathbf{x}$ is outside S, c equals $1/2$ if $\mathbf{x}$ tends to S from the inside of V, and c equals $-1/2$ if $\mathbf{x}$ tends to S from the outside of V. $T_{ij}(\mathbf{x}, \boldsymbol{\zeta})$ is the traction Green's function; i.e., the traction in direction i at point $\mathbf{x}$ of a point source in direction j applied at point $\boldsymbol{\zeta}$. The T_{ij} is found by application of Hooke's law to equation (1).

In the following sections, the displacement and traction Green's functions are first derived for use in finding the three-dimensional scattered field for a two-dimensional structure. Then, the procedure used to solve the problem of three-dimensional scattering by a two-dimensional topography is defined.

Green's Functions for Moving Point Sources in an Elastic Medium

The geometry of the problem is shown in Figure 1. A two-dimensional structure that is infinite in the di-
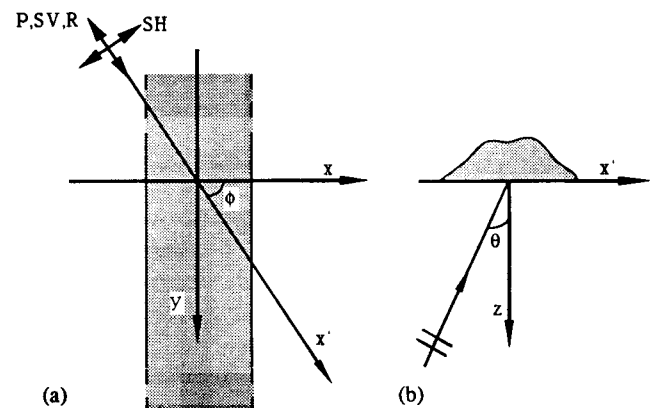

Figure 1. Geometry of the problem of scattering by two-dimensional topographies. (a) Horizontal plane; definition of azimuth ϕ. (b) Vertical plane; definition of incidence angle θ.

rection of the y axis is considered. The problem of three-dimensional scattering of plane waves by a two-dimensional structure is somewhat simpler than the full three-dimensional problem; at two cross sections perpendicular to the y axis the wave field will be identical but shifted in time. Point sources moving parallel to the y axis are therefore used to represent the diffracted field. This approach has also been used by Luco *et al.* (1990). The incoming wave arrives with an azimuth ϕ relative to the structure and an incidence θ to the vertical axis (see Fig. 1). It propagates with a velocity c. The wave has an apparent velocity c' along the y axis

$$c' = \frac{c}{\sin \phi \sin \theta} \qquad (3)$$

The scattered wave field can be expressed by point sources that move parallel to the y axis with a constant velocity c' along the interfaces of the model. In the case of a topography, the point sources move along the free surface.

To derive compact expressions for traction and displacement Green's functions for these moving point sources, one can start by solving the same problem for an acoustic medium. The solution g' to the inhomogeneous scalar wave equation for a fixed point source at the origin is given by

$$g' = \exp(i\omega t) \frac{\exp(-ikr)}{r}, \qquad (4)$$

where ω is the circular frequency, $k = \omega/V$ is the wavenumber, V is the acoustic wave propagation velocity, and r is the distance to the point source. This scalar Green's function can be expressed with a decomposition into plane waves (Weyl integral, see Aki and Richards, 1980)

$$g' = \exp(i\omega t) \frac{1}{2\pi}$$

$$\cdot \int_{-\infty}^{\infty} \int_{-\infty}^{\infty} \frac{\exp(-ik_x x - ik_y y - \gamma|z|)}{\gamma} dk_x dk_y, \qquad (5)$$

where k_x and k_y denote the x and y components of the wavenumber $\mathbf{k} = (k_x, k_y, i\gamma)^T$. The vertical wavenumber γ is defined as

$$\gamma = \sqrt{[k_x^2 + k_y^2 - (\omega/V)^2]} \quad \text{real } (\gamma) \geqq 0. \qquad (6)$$

The Green's function g is searched for a moving point source. To obtain g, the influence of the source is integrated over all positions ϵ along the y axis, taking into account the position of the source:

$$g = \int_{-\infty}^{\infty} d\epsilon \exp\left(i\omega\left(t - \frac{\epsilon}{c'}\right)\right) \frac{1}{2\pi}$$

$$\cdot \int_{-\infty}^{\infty} \int_{-\infty}^{\infty} \frac{\exp(-ik_x x - ik_y(y - \epsilon) - \gamma|z|)}{\gamma} dk_x dk_y. \qquad (7)$$

Integration over the space variable ϵ and substitution of v as ω/c' gives

$$g = \int_{-\infty}^{\infty} \int_{-\infty}^{\infty} \delta(v - k_y)$$

$$\cdot \exp(-ik_y y) \frac{\exp(-ik_x x - \gamma|z|)}{\gamma} dk_x dk_y, \qquad (8)$$

ignoring the factor $\exp(i\omega t)$. Integration over k_y yields

$$g = \int_{-\infty}^{\infty} \frac{\exp[-ik_x x - ivy - \sqrt{k_x^2 + (\omega/c')^2 - (\omega/V)^2}|z|]}{\sqrt{k_x^2 + (\omega/c')^2 - (\omega/V)^2}} dk_x. \qquad (9)$$

Rearrangement of equation (9) leads to

$$g = i \exp(-ivy)$$

$$\cdot \int_{-\infty}^{\infty} \frac{\exp[-ik_x x - i\sqrt{(\omega/V)^2 - k_x^2 - v^2}|z|]}{\sqrt{(\omega/V)^2 - k_x^2 - v^2}} dk_x \qquad (10)$$

with

$$Im\left[\sqrt{(\omega/V)^2 - k_x^2 - v^2}\right] \leqq 0.$$

This integral is the plane wave decomposition of the wave field radiated by a moving point source. It can be expressed using Lamb's (1904) representation for Hankel functions as

$$g = \pi i \exp(-ivy) H_0^{(1)}\left(\sqrt{k^2 - v^2} R\right) \qquad (11)$$

with

$$R = \sqrt{(x - x')^2 + (z - z')^2}, \qquad (12)$$

where (x', z') is the source location in the $(x - z)$ plane.

It is possible to express directly the equivalent of equation (11) for an elastic material with density ρ by (Morse and Feshbach, 1953; Pao and Varatharajulu, 1976)

$$G_{ij}(\mathbf{x}, \zeta) = \frac{1}{4\pi\rho\omega^2} \left\{ k_s g_s(\mathbf{x}, \zeta)\delta_{ij} \right.$$

$$\left. + \frac{\delta^2}{\delta x_i \delta x_j} [g_p(\mathbf{x}, \zeta) - g_s(\mathbf{x}, \zeta)] \right\}, \quad (13)$$

where indices s and p refer to shear and compressional waves, respectively.

The insertion of equation (12) in equation (13) gives the required displacement Green's functions. As discussed earlier, traction Green's functions can be obtained by applying Hooke's law. The compact expressions for the Green's functions are given in the Appendix.

These expressions were validated by comparison with well-known expressions of Green's functions in three dimensions. The spatial Fourier transform over y of the latter provides $G_{ij}(x, k_y, z, \omega)$ by replacing k_y by ω/c'.

Implementation of the Method

In implementing the method, the total wave field is assumed to be the superposition of the diffracted field and the "free field" u°; i.e., the field in the absence of the irregularity. The definition of the free field is addressed later in this section.

Under this assumption, equation (1) becomes

$$u_i(\mathbf{x}) = u_i^\circ(\mathbf{x}) + \int_s \psi_j(\zeta)G_{ij}(\mathbf{x}, \zeta) \, dS_\zeta. \quad (14)$$

At the free surface, tractions vanish. Denoting tractions of the free field t°, this condition gives

$$\frac{1}{2} \psi_i(\mathbf{x}) + \int_s \psi_j(\zeta)T_{ij}(\mathbf{x}, \zeta) \, dS_\zeta = -t_i^\circ(\mathbf{x}). \quad (15)$$

This continuous integral must be replaced by a discrete one for computer-based analysis. Again, the methodology of Sánchez-Sesma and Campillo (1991) was followed: the surface is discretized into N segments of equal length Δs. For each frequency, N is chosen so that Δs is much smaller than the wavelength of the shear waves. Consequently, the force density $\psi_i(\mathbf{x})$ is chosen to be constant on each of the segments. Testing of the discretization parameters showed that five segments per wavelength is sufficient to ensure accurate results. A finite portion of the surface is discretized. A discretization of five times the length L of the irregularity, as used in the results presented here, yielded results within a few percent of those obtained by discretizing $3L$ of the surface.

A discrete version of equation (15) can be used to find the surface force $\psi_i(\zeta_l)$ on each segment. The evaluation of the traction at the center of each segment leads to the system of linear equations

$$\sum_{l=1}^{N} \psi_j(\zeta_l)t_{ij}(\mathbf{x}_n, \zeta_l) = -t_i^\circ(\mathbf{x}_n) \quad n = 1, N \quad (16)$$

where

$$t_{ij}(\mathbf{x}_n, \zeta_l) = \frac{1}{2} \delta_{ij}\delta_{nl} + \int_{\zeta_l - \Delta s/2}^{\zeta_l + \Delta s/2} T_{ij}(\mathbf{x}_n, \zeta_l)dS_\zeta \quad (17)$$

The integral in equation (17) is evaluated by Gaussian integration, except when $n = l$. In this particular case, it is calculated analytically by using ascending series for Bessel functions (e.g., Abramowitz and Stegun, 1972).

Once $\psi_i(\zeta_l)$ has been found by resolution of the system of equations (16), the displacement at any point can be evaluated by the following discrete equivalent of equation (14):

$$u_i(\mathbf{x}) = u_i^\circ(\mathbf{x}) + \sum_{l=1}^{N} \psi_j(\zeta_l)g_{ij}(\mathbf{x}, \zeta_l), \quad (18)$$

where

$$g_{ij}(\mathbf{x}, \zeta_l) = \int_{\zeta_l - \Delta s/2}^{\zeta_l + \Delta s/2} G_{ij}(\mathbf{x}, \zeta_l)dS_\zeta. \quad (19)$$

If $\mathbf{x}$ is located on the surface, the integral is again evaluated by analytical expressions over the segment on which $\mathbf{x}$ is located. Gaussian integration is used on other segments.

This section is concluded by a short discussion of the definition of the free fields u° and t°. In the examples presented in the next sections, a free field is used that includes the reflection of the incoming wave on the free surface of the half-space. For ridges, this field is extended analytically to the points on the ridge that are located outside the reference half-space. This procedure has the advantage of reducing boundary effects due to the truncation of the model; the surface forces ψ_i will decrease in amplitude toward the limits of the model because the effect of the irregularity decreases. On the other hand, the analytically extended field is both nonphysical and noncausal. For strongly antisymmetrical ridges, we encounter problems in the form of noncausal arrivals when we use the half-space reference field. Use of the full space free field solves these problems but introduces artifacts in the form of reflections on the boundary of the model.

For canyons, analytical expressions for Rayleigh waves are used to define the free field. The problem of defining the free field for incoming Rayleigh waves on ridges is not addressed, as the exponential decrease with depth of the amplitude of Rayleigh waves leads to numerical problems for high frequencies when the analyt-

ical expression is extended upward. For the two-dimensional case, the Rayleigh waves can be simulated by a vertical point load applied far from the topographic relief (Sánchez-Sesma and Campillo, 1991).

Validation of the Method

The two-dimensional case is a limiting case of the method ($\phi = 0°$). In this case, the Green's functions listed in the Appendix are equivalent to well-known two-dimensional compact expressions for Green's functions (e.g., Sánchez-Sesma and Campillo, 1991). Our results agree with those of Sánchez-Sesma and Campillo (1991) for the two-dimensional case where the two methods are strictly equivalent. As Sánchez-Sesma and Campillo (1991) have compared their results to those of other authors, the two-dimensional case is not addressed further here, and the reader is referred to Sánchez-Sesma and Campillo (1991).

Literature on three-dimensional scattering by two-dimensional topographies is scarce. We compared our results with those of Luco *et al.* (1990) using the model depicted in Figure 2. The topographic irregularity is a semi-circular canyon of radius a in a homogeneous half-space. The half-space is characterized by a shear-wave velocity β and a compressional-wave velocity $\alpha = 2\beta$. Figure 3 shows the comparison with Luco *et al.* for an incident P wave arriving with an azimuth of 45° and an incidence angle of 45° for three normalized frequencies η where

$$\eta = \frac{\omega a}{\pi \beta}. \qquad (20)$$

For $\eta = 1$, the shear wavelength equals the diameter of the canyon.

The agreement between our results and those of Luco *et al.* (1990) is generally good. Especially at low frequencies, the agreement is excellent, while small differences arise at higher frequencies. The level of amplification and deamplification are slightly different across the topography, while the general shape of the curves is similar.
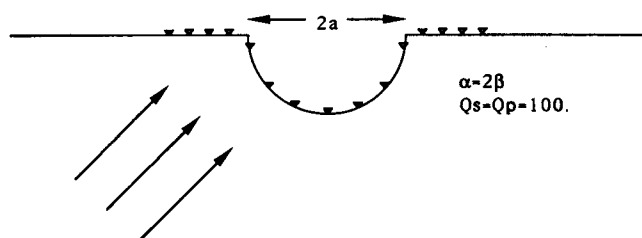
Figure 2. Model of the semi-circular canyon used in the simulations.

Numerical Results

Parameters for simulations of a wave field scattered by a two-dimensional topography include the geometry, the elastic parameters of the model, the type of the incident plane wave (P, SV, SH, Rayleigh), its azimuth ϕ, and incidence θ with respect to the z axis. Simulations were performed for incident P, SV, SH, and Rayleigh waves (except for Rayleigh waves incident on a ridge). Selected results are presented here for simulations with two simple geometries (semi-circular canyon, semi-circular ridge) and two types of incident waves (P and SV waves). Results will be presented in both the space-time (x, t) and in the space-frequency (x, η) domains for $-2 \leq x/a \leq 2$, where a is the radius of the canyon or the ridge. The normalized frequency η, defined previously, is used. Simulations were carried out between $\eta = 0$ and $\eta = 6.4$. Traces in time were obtained by convolution with a Ricker wavelet of central frequency $\eta = 2$, fol-
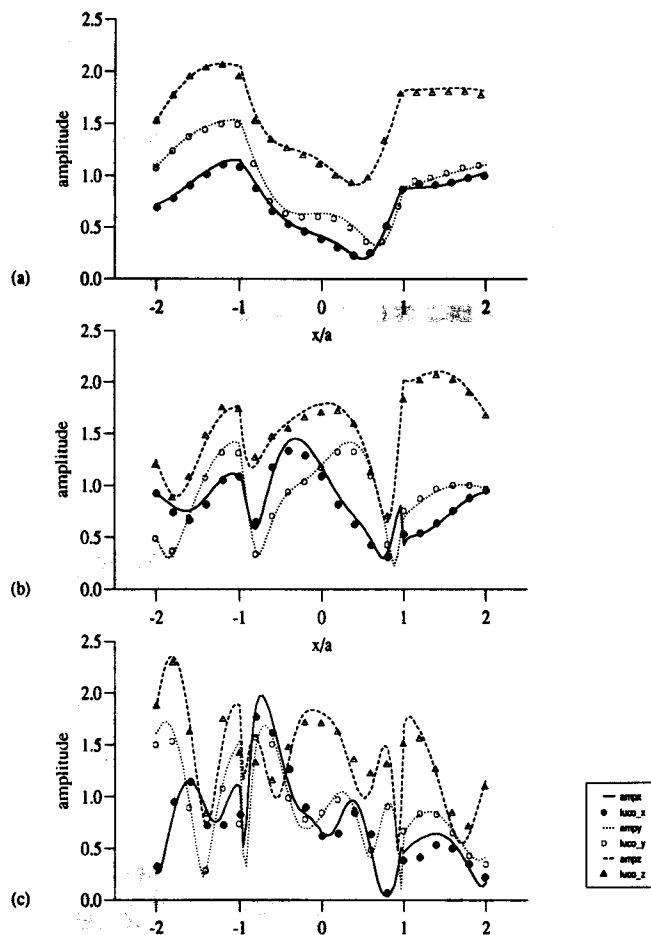
Figure 3. Example of comparison of obtained results with those of Luco *et al.* (1990). Continuous lines, dotted lines, and dashed lines; our results. Solid circles, open circles, and triangles; Luco *et al.* (1990). (a) $\eta = 0.5$, (b) $\eta = 1$, and (c) $\eta = 2$.
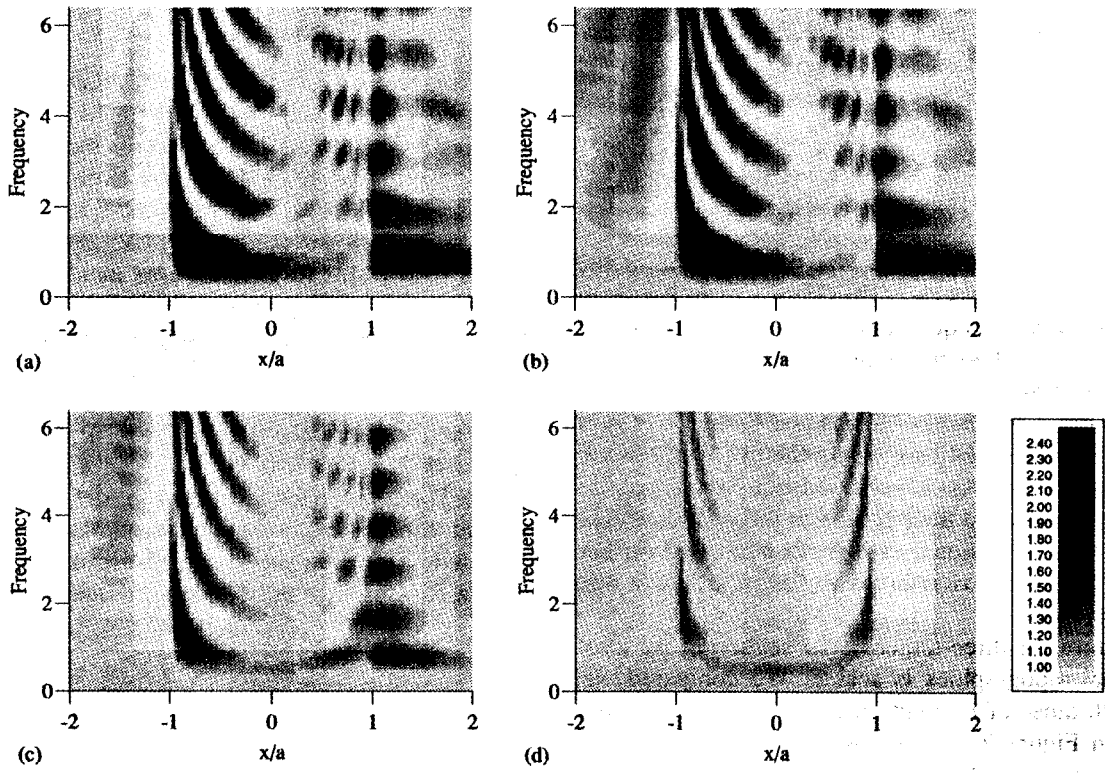
Figure 4. Spectral amplitude of total horizontal displacements across the semi-circular canyon. Incident wave field, *SV* wave with $\theta = 45°$. (a) $\phi = 0°$, (b) $\phi = 30°$, (c) $\phi = 60°$, and (d) $\phi = 90°$.
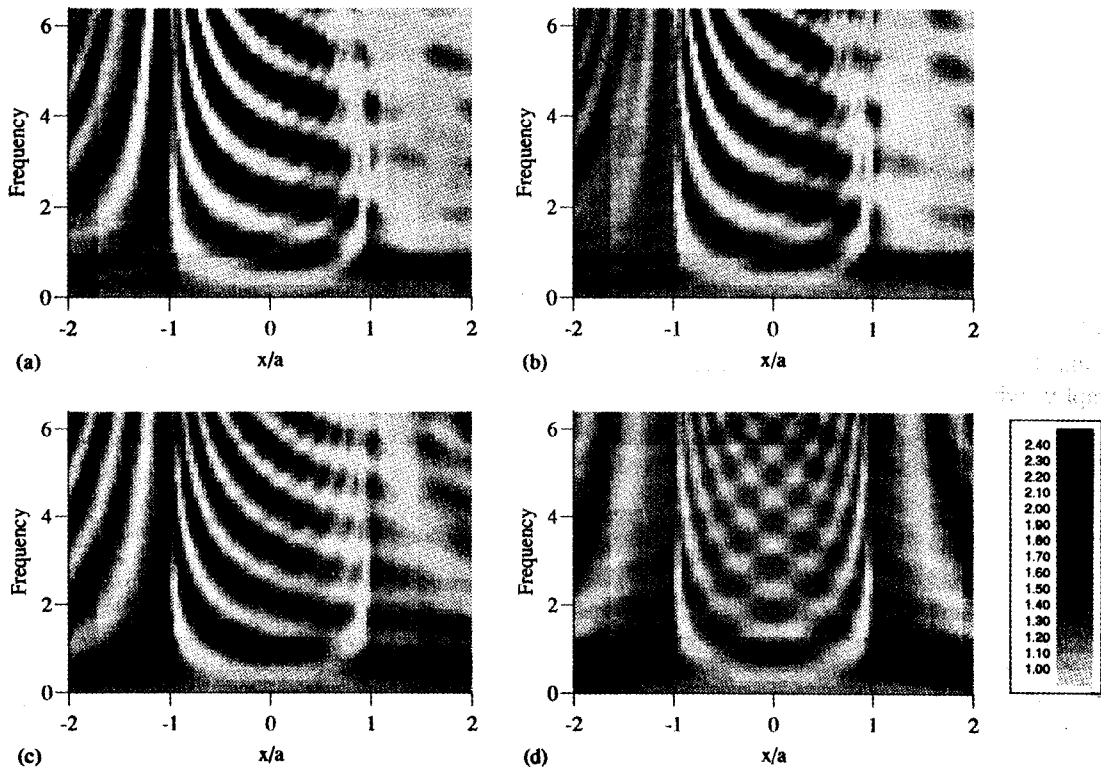

Figure 5. Same as Figure 4 for vertical displacements.

lowed by an inverse Fourier transform. The amplitude scale is the same in all synthetic seismograms shown in this article.

Semi-Circular Canyon

In the case of the semi-circular canyon, the model presented in Figure 2 was used with only one difference compared to the previous simulations: in the following, the quality factor for shear and compressional waves is 1000. Figures 4 and 5 show the (x, η) image of the wave field across the canyon for an incident SV wave with incidence $\theta = 45°$ and differing azimuths ($\phi = 0°$, $30°$, $60°$, and $90°$). Figure 4 shows the total horizontal displacement and Figure 5 the vertical displacement.

As the azimuth increases, the amplitude of the scattering changes. Figures 4 and 5 show that for small and intermediate azimuths ($\phi \leqq 60°$), it is dominated by scattering generated by the edge of the canyon at $x/a = -1$. The vertical displacement for $\phi = 90°$ shows clearly how the scattered field across the canyon is the result of interference between scattered waves generated at the edges. Spectral amplitudes generally seem to decrease as the azimuth of the incident wave increases.

The synthetic seismograms for the four azimuths (Figs. 6 through 9) show that the scattered field is mainly composed of creeping waves across the canyon, while outside the canyon the scattered waves are mostly Rayleigh waves and waves reflected by the surface of the canyon. The general image seems to be the same for all azimuths, but the relative amplitudes and the apparent velocity of the diffracted waves are strongly dependent on the azimuth. Diffraction is less for an azimuth of 90°, but amplitudes can nevertheless be high at specific points because of the interference of waves. Even when the incident wave field has displacements only along the y and z axis, the scattered field has significant displacements on the x component.

The apparent velocity of the diffracted waves can be understood by considering the meaning of c', the apparent velocity along the y axis, in a simplified way using Huygen's principle. The c' can take any value between c_R and infinity, where c_R is the Rayleigh wave velocity in the half-space. The source emits S and P waves, with velocities c_β and c_α. If c' is greater than c_α, the field of the moving point source corresponds to supersonic waves. This situation is illustrated in Figure 10a. The resulting wave front moves with an angle ϕ' to the y axis, where

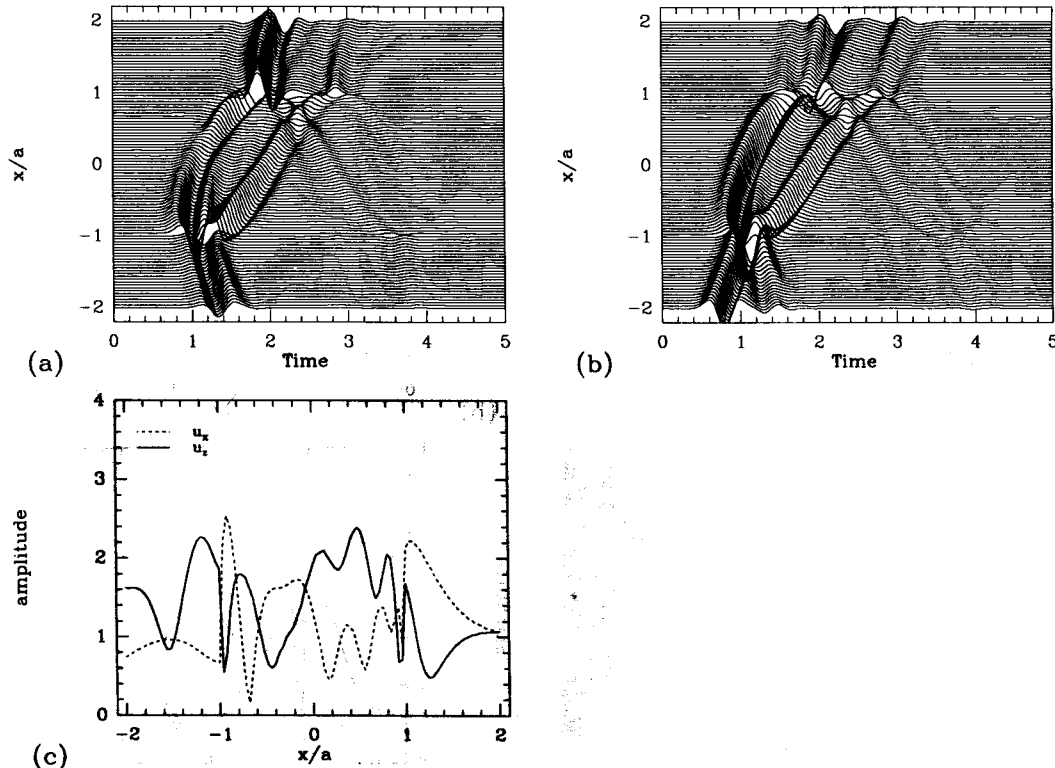$$\cos \phi' = \frac{c_{\alpha,\beta}}{c'} = \frac{c_{\alpha,\beta}}{c} \sin \theta \sin \phi. \qquad (21)$$

Figure 6. Displacement amplitudes across a semi-circular canyon. Incident wave field, SV wave with $\phi = 0°$ and $\theta = 45°$. (a) Synthetic seismograms, u_x, (b) synthetic seismograms, u_z, and (c) spectral amplitudes for $\eta = 2$.
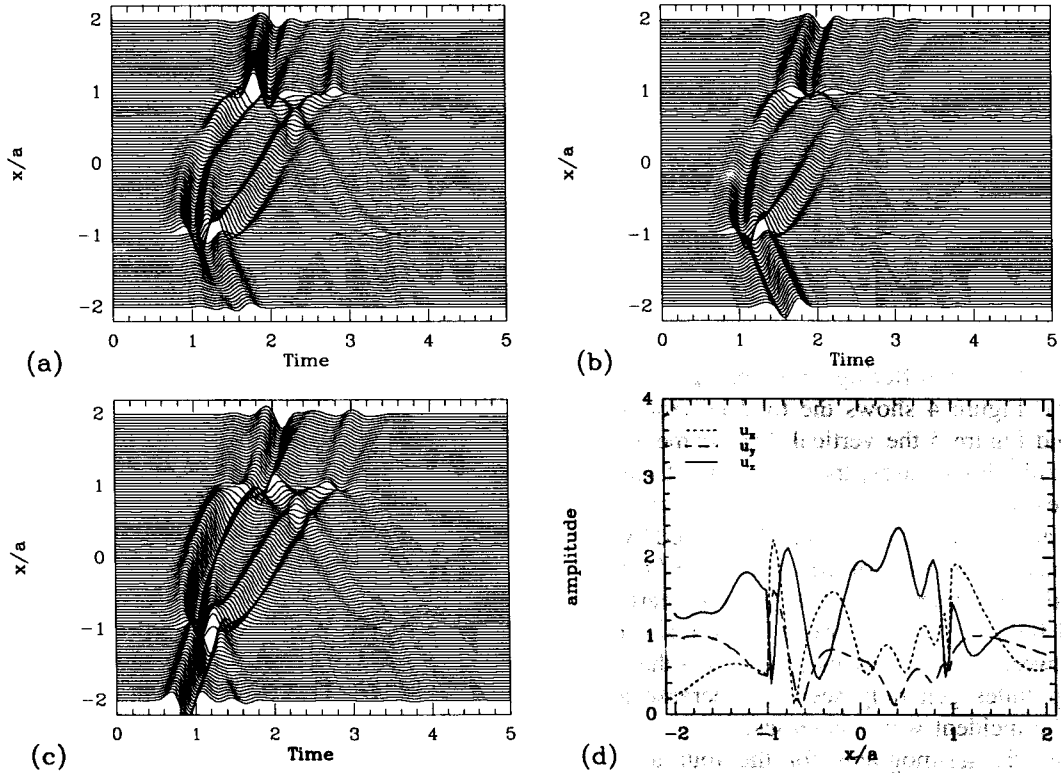
Figure 7. Same as Figure 6 with $\phi = 30°$. (a) Synthetic seismograms, u_x, (b) synthetic seismograms, u_y, (c) synthetic seismograms, u_z, and (d) spectral amplitudes for $\eta = 2$.
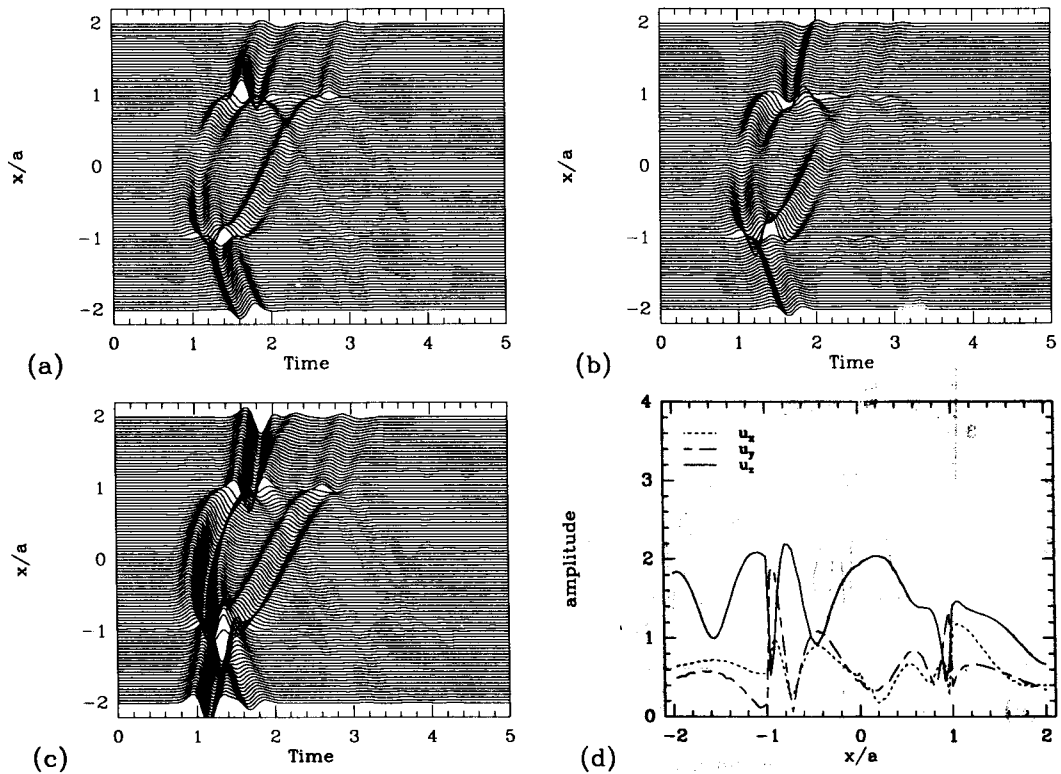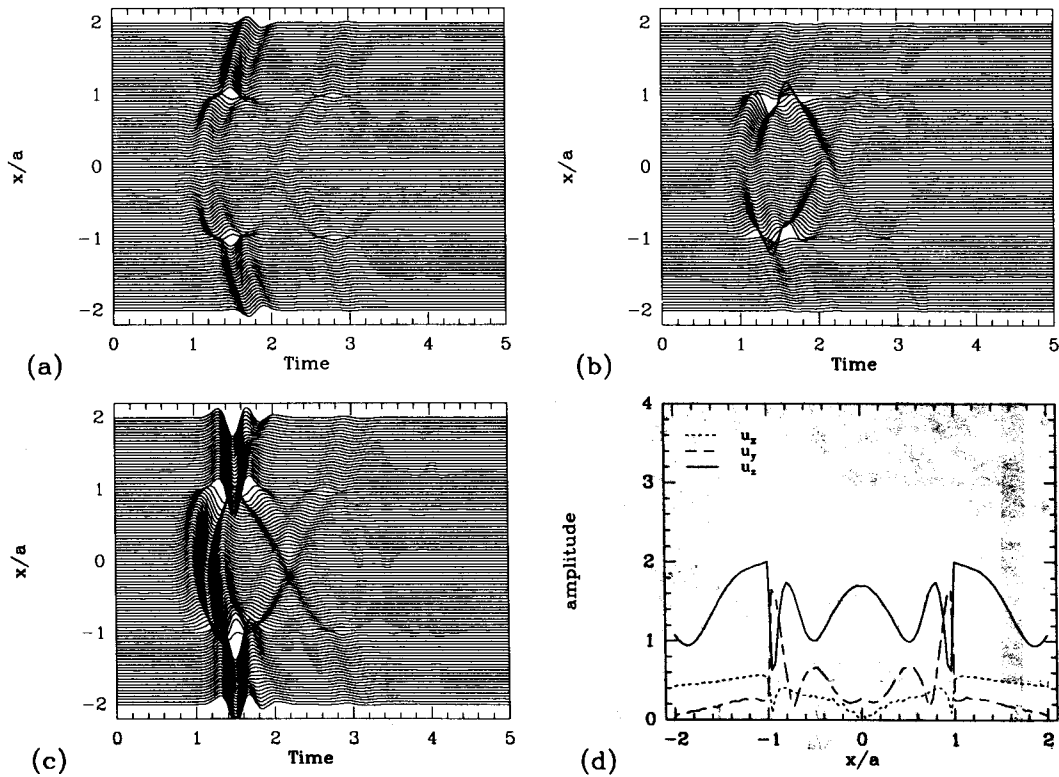

Figure 8. Same as Figure 7 with $\phi = 60°$.

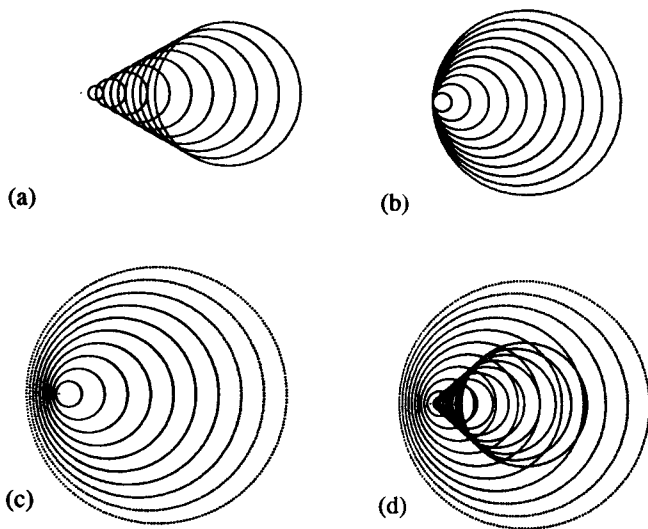Figure 9. Same as Figure 7 with $\phi = 90°$.

Figure 10. Simplified wave field radiated by a source moving with constant velocity c in medium of wave propagation velocities $V_{\alpha,\beta}$. (a) $c > V_{\alpha,\beta}$, (b) $c = V_{\alpha,\beta}$, (c) $c < V_{\alpha,\beta}$, and (d) $V_\beta < c < V_\alpha$.

The use of these simple formulas to explain the apparent velocity of the diffracted waves was verified in several examples. They also explain why the scattered wave field almost equals the superposition of the two-dimensional in-plane and out-of-plane solutions (Pei and Papageorgiou, 1993a) when the incident waves arrive almost vertically (θ is small).

There is clearly a singularity when c' equals c_α or c_β. This is illustrated in Figure 10b. The singularity is, in fact, weak, as the Green's functions near the source can be integrated. Simulations with c' slightly smaller and greater than c_α and c_β confirmed that there is no particular effect to expect in practice in that particular situation. The wave field of the moving source when $c' < c_\beta$ is illustrated in Figure 10c. No plane wave is created and the wave field presents a "Doppler effect." The absence of a clearly defined wave front may explain why diffraction seems to decrease for large azimuths. When $c_\beta < c' < c_\alpha$, the situation is a mixture of the supersonic and the subsonic case, as illustrated in Figure 10d.

Semi-Circular Ridge

The various parameters of the model of a semi-circular ridge are identical to the model of the semi-circular canyon; the models differ only by the sign of the topography. In this section, we show examples of scattering
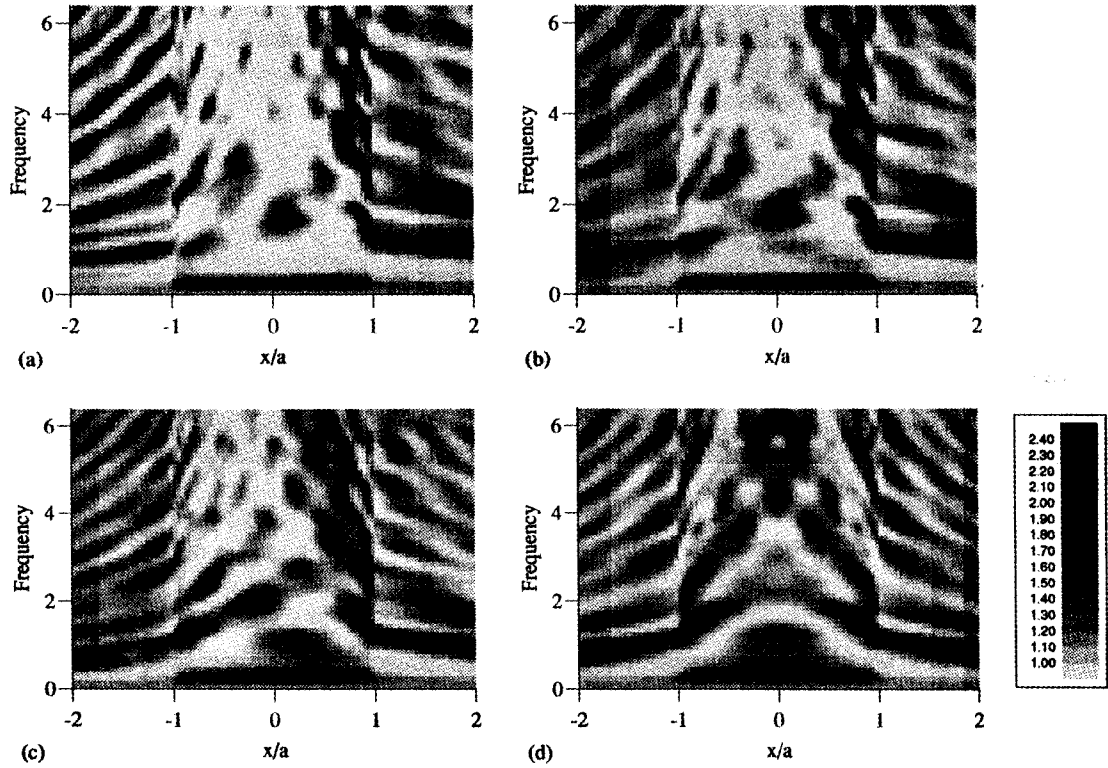
The apparent velocity c_x along the x axis of this wave front is consequently

$$c_x = \frac{c_{\alpha,\beta}}{\sin \phi'}. \tag{22}$$

Figure 11. Spectral amplitude of horizontal displacements across a semi-circular ridge. Incident wave field, P wave with $\theta = 45°$. (a) $\phi = 0°$, (b) $\phi = 30°$, (c) $\phi = 60°$, and (d) $\phi = 90°$.
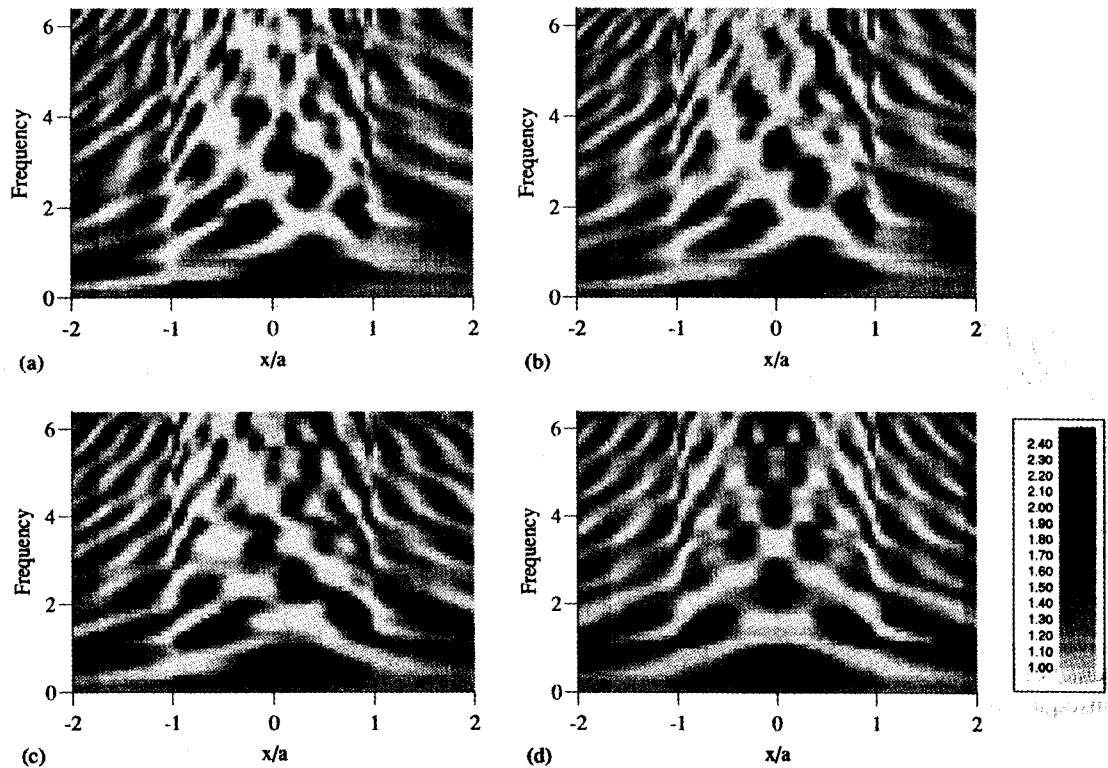

Figure 12. Same as Figure 11 for vertical displacements.

by the ridge of a plane P wave with an incidence θ of 45° to the z axis.

Figures 11 and 12 show results of these simulations for various azimuths of the incident P wave ($\phi = 0°$, 30°, 60°, and 90°). Total horizontal displacement is shown in Figure 11 and vertical displacement in Figure 12. For all azimuths, the interference is significant. Apparently, scattered waves are created by both edges of the canyon and the interference pattern is very complicated. The amplitude of horizontal displacement is far from being symmetrical over the ridge when the azimuth is small; it is generally greatest near the far corner of the ridge ($x/a = 1$).

The synthetic seismograms for $\phi = 0°$ and 90° are shown in Figures 13 and 14, respectively. Analysis of the apparent velocities of the scattered waves indicate that creeping shear waves are generated at both edges of the ridge. The P waves are reflected away from the ridge at $x/a = -1$ and into the ridge near $x/a = 1$. The time duration of the signal is long because scattered waves bounce back and forth across the ridge.

Conclusions

An indirect boundary element method was presented for calculating the three-dimensional scattered wave field of plane waves incident on a two-dimensional topography. Results were presented in the frequency and time domains for two topographies of simple geometry: a semicircular canyon and a semi-circular ridge. The signal to noise ratio of the synthetic seismograms was in general very low, so it was possible to interpret not only the amplification of the incident waves, but also the nature of the scattered wave field. The interpretations are based upon analysis of particle motions and apparent velocities of the waves. The total scattered wave field presents a complicated pattern of amplification and deamplification because it is the result of interference between different scattered waves: Rayleigh waves, reflected compressional and shear waves, and creeping waves. The complexity does not seem to change considerably when the incident plane waves arrive outside the symmetry axis of the topography. The points where amplification or deamplification occur change as a function of geometry, azimuth, incidence angle, and type of incident wave field, but the general level of amplification does not change significantly. Of all the simulations that we performed, the maximum spectral amplification of displacement was 4.9 (for Rayleigh waves, the reference value is the horizontal motion, which is assumed to be unitary). The simulations also showed that there is, in practice, no particular effect when the incident wave field is such that
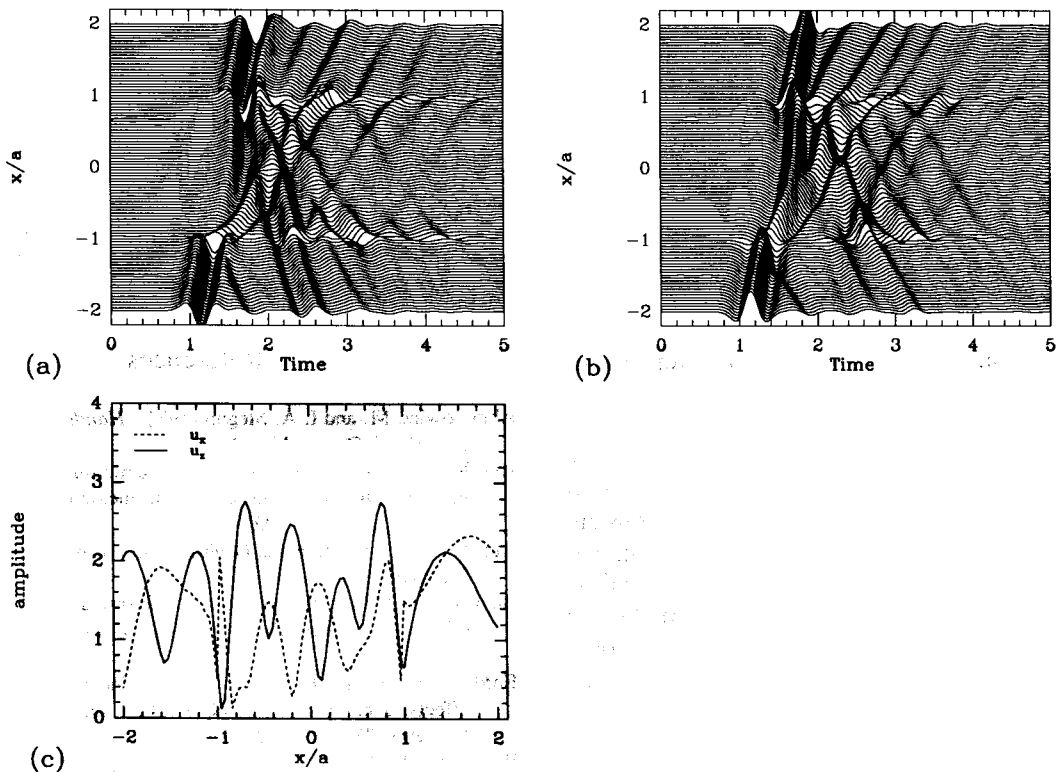

Figure 13. Displacement amplitudes across a semi-circular ridge. Incident wave field, P wave with $\phi = 0°$ and $\theta = 45°$. (a) Synthetic seismograms, u_x, (b) synthetic seismograms, u_z, and (c) spectral amplitudes for $\eta = 2$.
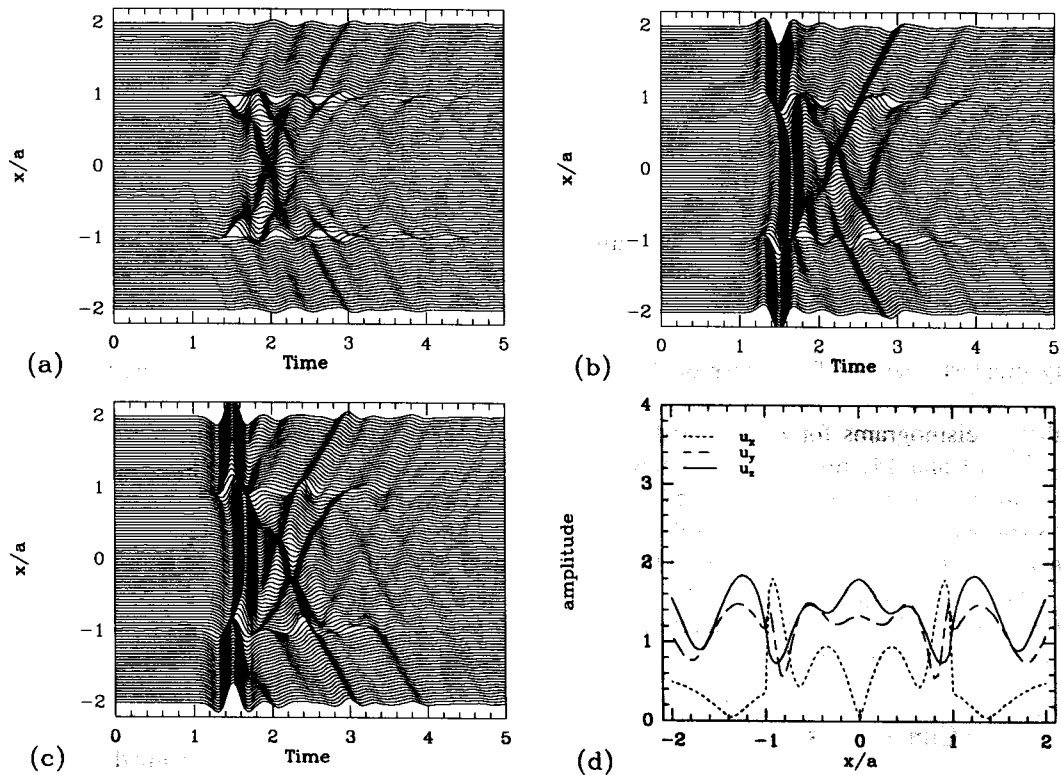
Figure 14.   Same as Figure 13 with $\phi = 90°$. (a) Synthetic seismograms, u_x, (b) synthetic seismograms, u_y, (c) synthetic seismograms, u_z, and (d) spectral amplitudes for $\eta = 2$.

there is a singularity in the Green's function for a moving point source.

Our results indicate that in the three-dimensional case, as in the two-dimensional one, the wave field scattered by a topography is significant over large distances. Of course, the introduction of damping in the model will diminish this effect; nevertheless, it is not surprising to find extreme values of spectral ratios between the top and the base of mountains. Peaks in the spectral ratio are expected for frequencies where deamplification takes place at the reference station; there is no theoretical evidence, however, of broadband amplification at any location on the topography.

We needed to make only one approximation for the implementation of the method: we divided the topography into a number of segments, each with a constant force distribution. Tests showed that five segments per wavelength is sufficient to obtain a good accuracy of the results. In this way, performing each of the simulations presented here requires only a few hours CPU time on a medium-sized workstation (IBM Risc 6000, 9 Mflops). The low computation time means that the method can be extended to more complex problems, such as scattering of plane waves by alluvial valleys or propagation of crustal phases across large structures. Direct use of the method presented in this article could be parametric studies or modeling of observed topographic effects.

Acknowledgments

References

Abramowitz, M. and I. A. Stegun (1972). *Handbook of Mathematical Functions*, Dover, New York.

Aki, K. and K. L. Larner (1970). Surface motion of a layered medium having an irregular interface due to incident plane SH waves, *J. Geophys. Res.* **75**, 1921–1941.

Aki, K. and P. G. Richards (1980). *Quantitative Seismology*, W. H. Freeman, San Francisco.

Bard, P.-Y. (1982). Diffracted waves and displacement field over two-dimensional elevated topographies, *Geophys. J. R. Astr. Soc.* **71**, 731–760.

Bard, P.-Y. and E. T. Tucker (1985). Underground and ridge site effects: a comparison of observation and theory, *Bull. Seism. Soc. Am.* **75**, 905–922.

Bouchon, M. (1973). Effect of topography on surface motion, *Bull. Seism. Soc. Am.* **63**, 615–632.

Bouchon, M. (1985). A simple, complete numerical solution to the problem of diffraction of SH waves by an irregular surface, *J. Acoust. Soc. Am.* **77**, 1–5.

Davis, L. L. and L. R. West (1973). Observed effects of topography on ground motion, *Bull. Seism. Soc. Am.* **63**, 283–298.

Geli, L., P.-Y. Bard, and B. Jullien (1988). The effect of topography on earthquake ground motion: a review and new results, *Bull. Seism. Soc. Am.* **78**, 42–63.

Griffiths, D. W. and G. A. Bollinger (1979). The effect of Appalachian mountain topography on seismic waves, *Bull. Seism. Soc. Am.* **69**, 1081–1105.

Kawase, H. (1988). Time-domain response of a semicircular canyon for incident SV, P, and Rayleigh waves calculated by the discrete wavenumber boundary element method, *Bull. Seism. Soc. Am.* **78**, 1415–1437.

Khair, K. R., S. K. Datta, and A. H. Shah (1989). Amplification of obliquely incident seismic waves by cylindrical alluvial valleys of arbitrary cross-sectional shape, Part I, Incident P and SV waves, *Bull. Seism. Soc. Am.* **79**, 610–630.

Khair, K. R., S. K. Datta, and A. H. Shah (1991). Amplification of obliquely incident seismic waves by cylindrical alluvial valleys of arbitrary cross-sectional shape, Part II, Incident SH and Rayleigh waves, *Bull. Seism. Soc. Am.* **81**, 346–357.

Kupradze, V. D. (1963). *Dynamical problems in elasticity*, in *Progress in Solid Mechanics*, Vol. 3, I. N. Sneddon and R. Hill (Editors), North-Holland, Amsterdam.

Lamb, H. (1904). On the propagation of tremors over the surface of an elastic solid, *Philos. Trans. R. Soc. London*, Ser. A **203**, 1–42.

Lee, V. W. and H. Cao (1989). Diffraction of SV waves by circular canyons of various depths, *J. Eng. Mech. Am. Soc. Civil. Eng.* **115**, 2035–2056.

Liu, S. W., S. K. Datta, and M. Bouden (1991). Scattering of obliquely incident seismic waves by a cylindrical valley in a layered half-space, *Int. J. Earthquake Eng. Struct. Dyn.* **20**, 859–870.

Luco, J. E., H. L. Wong, and F. C. P. De Barros (1990). Three-dimensional response of a cylindrical canyon in a layered half-space, *Int. J. Earthquake Eng. Struct. Dyn.* **19**, 799–817.

Morse, P. M. and H. Feshbach (1953). *Methods of Mathematical Physics, Part II*, McGraw-Hill, New York.

Pao, Y.-H. and V. Varatharajulu (1976). Huygens' principle, radiation conditions, and integral formulas for the scattering of elastic waves, *J. Acoust. Soc. Am.* **59**, 1361–1371.

Pei, D. and A. S. Papageorgiou (1993a). Three-dimensional response of an infinitely long cylindrical canyon to obliquely incident seismic waves (abstract), *Seism. Res. Lett.* **64**, 27.

Pei, D. and A. S. Papageorgiou (1993b). Study of the response of cylindrical alluvial valleys of arbitrary cross-section to obliquely incident seismic waves using the discrete wavenumber boundary element method, in *Soil Dynamics and Earthquake Engineering VI*, A. S. Cakmak and C. A. Brebbia (Editors), Comp. Mech. Publications—Elsevier Appl. Sc., Southampton–London, 149–161.

Sánchez-Sesma, F. J. and M. Campillo (1991). Diffraction of P, SV, and Rayleigh waves by topographical features: a boundary integral formulation, *Bull. Seism. Soc. Am.* **81**, 2234–2253.

Sánchez-Sesma, F. J. and M. Campillo (1993). Topographic effects for incident P, SV, and Rayleigh waves, *Tectonophysics, 218*, 113–125.

Sánchez-Sesma, F. J. and E. Rosenblueth (1979). Ground motion on alluvial valleys under incident plane SH waves. *Int. J. Earthquake Eng. Struct. Dyn.* **7**, 441–450.

Todorovska, M. I. and V. W. Lee (1990). A note on response of shallow circular valleys to Rayleigh waves: analytical approach, *Earthquake Eng. Eng. Vibration* **10**, 21–34.

Todorovska, M. I. and V. W. Lee (1991). Surface motion of circular valleys of variable depth for incident plane SH waves, *Soil Dyn. Earthquake Eng.* **10**, 192–200.

Trifunac, M. D. (1973). Scattering of plane SH waves by a semi-
cylindrical canyon, *Int. J. Earthquake Eng. Struct. Dyn.* **1**, 267–281.

Wong, H. L. (1982). Effect of surface topography on the diffraction of P, SV, and Rayleigh waves, *Bull. Seism. Soc. Am.* **72**, 1167–1183.

Wong, H. L. and P. C. Jennings (1975). Effect of canyon topographies on strong ground motion, *Bull. Seism. Soc. Am.* **65**, 1239–1257.

Zhang, L. and A. K. Chopra (1991). Three-dimensional analysis of spatially varying ground motions around a uniform canyon in a homogeneous half-space, *Int. J. Earthquake. Eng. Struct. Dyn.* **20**, 911–926.

Appendix

Green's Functions for a Moving Point Source in an Elastic Unbounded Medium

Consider a point source moving in a homogeneous isotropic elastic unbounded medium with density ρ, Lamé constants μ and λ, and shear- and compressional-wave velocities α and β, respectively. The point source moves with velocity c parallel to the x_2 axis along the line through $(x_1^0, 0, x_3^0)$. The observation point is situated at (x_1, x_2, x_3). The term $i^2 = -1$, $t =$ time, $\omega =$ circular frequency, and $H_m^{(2)}$ is the Hankel functions of the second kind and order m. Other notations used are

$$R = \sqrt{(x_1 - x_1^0)^2 + (x_3 - x_3^0)^2},$$

$$\gamma_1 = \frac{x_1 - x_1^0}{R}, \quad \gamma_3 = \frac{x_3 - x_3^0}{R}$$

$$q = \frac{\omega}{\alpha}, \quad k = \frac{\omega}{\beta}, \quad v = \frac{\omega}{c}$$

$$Q = \sqrt{q^2 - v^2} = \omega \sqrt{\frac{1}{\alpha^2} - \frac{1}{c^2}},$$

$$K = \sqrt{k^2 - v^2} = \omega \sqrt{\frac{1}{\beta^2} - \frac{1}{c^2}}$$

with

$$\mathrm{Imag}(Q) \leqq 0; \quad \mathrm{Imag}(K) \leqq 0$$

$$A = \left(\frac{1}{\alpha^2} - \frac{1}{c^2}\right) H_0^{(2)}(QR) + \left(\frac{1}{\beta^2} + \frac{1}{c^2}\right) H_0^{(2)}(KR)$$

$$B = \left(\frac{1}{\alpha^2} - \frac{1}{c^2}\right) H_2^{(2)}(QR) - \left(\frac{1}{\beta^2} - \frac{1}{c^2}\right) H_2^{(2)}(KR)$$

$$C = \sqrt{\frac{1}{\beta^2} - \frac{1}{c^2}} H_1^{(2)}(KR) - \sqrt{\frac{1}{\alpha^2} - \frac{1}{c^2}} H_1^{(2)}(QR)$$

$$E = \left(\frac{1}{\beta^2} - \frac{1}{c^2}\right) H_0^{(2)}(KR) - \left(\frac{1}{\alpha^2} - \frac{1}{c^2}\right) H_0^{(2)}(QR)$$

$$D(z) = zH_1^{(2)}(z).$$

The Green's functions for harmonic time dependence exp $(i\omega t)$ of the moving point source can be expressed by the following compact forms:

$$G_{ij} = \frac{1}{8i\rho}[\delta_{ij}A - (2\gamma_i\gamma_j - \delta_{ij})B]\exp(-ivx_2),$$

$$i,j = 1, 3$$

$$G_{2j} = G_{j2} = \frac{1}{4\rho c}\left[\sqrt{\frac{1}{\beta^2} - \frac{1}{c^2}}H_1^{(2)}(KR)\right.$$

$$\left. - \sqrt{\frac{1}{\alpha^2} - \frac{1}{c^2}}H_1^{(2)}(QR)\right]\gamma_j\exp(-ivx_2), \quad j = 1, 3$$

$$G_{22} = \frac{1}{4i\rho}\left[\left(\frac{1}{\beta^2} - \frac{1}{c^2}\right)H_0^{(2)}(KR) + \frac{1}{c^2}H_0^{(2)}(QR)\right]$$

$$\cdot \exp(-ivx_2)$$

$$T_{11} = \lambda e_1 n_1 + \mu(\epsilon_{111}n_1 + \epsilon_{131}n_3)$$

$$T_{31} = \lambda e_1 n_3 + \mu(\epsilon_{131}n_1 + \epsilon_{331}n_3)$$

$$T_{13} = \lambda e_3 n_1 + \mu(\epsilon_{113}n_1 + \epsilon_{133}n_3)$$

$$T_{33} = \lambda e_3 n_3 + \mu(\epsilon_{133}n_1 + \epsilon_{333}n_3)$$

$$T_{12} = \lambda e_2 n_1 + \mu(\epsilon_{112}n_1 + \epsilon_{132}n_3)$$

$$T_{21} = \mu(\epsilon_{121}n_1 + \epsilon_{231}n_3)$$

$$T_{32} = \lambda e_2 n_3 + \mu(\epsilon_{132}n_1 + \epsilon_{332}n_3)$$

$$T_{23} = \mu(\epsilon_{123}n_1 + \epsilon_{233}n_3)$$

$$T_{22} = \mu(\epsilon_{122}n_1 + \epsilon_{232}n_3)$$

where

$$\epsilon_{ijk} = \frac{\delta G_{ik}}{\delta x_j} + \frac{\delta G_{jk}}{\delta x_i}$$

$$e_i = \frac{i}{4\rho R}\exp(-ivx_2)\gamma_i\frac{D(QR)}{\alpha^2}, \quad i = 1, 3$$

$$e_2 = -\frac{i}{4\rho}\exp(-ivx_2)\frac{\omega}{c\alpha^2}H_0^{(2)}(QR)$$

$$\epsilon_{111} = \exp(-ivx_2)\frac{i}{4\rho R}\gamma_1\left\{2\left(\frac{1}{\alpha^2} - \frac{1}{c^2}\right)\gamma_1^2 D(QR)\right.$$

$$+ 2\left(\frac{1}{\beta^2} - \frac{1}{c^2}\right)\gamma_3^2 D(KR)$$

$$\left. + 2(3\gamma_3^2 - \gamma_1^2)B + \frac{2}{c^2}D(KR)\right\}$$

$$\epsilon_{131} = \exp(-ivx_2)\frac{i}{4\rho R}\gamma_3\left\{2\left(\frac{1}{\alpha^2} - \frac{1}{c^2}\right)\gamma_1^2 D(QR)\right.$$

$$+ \left(\frac{1}{\beta^2} - \frac{1}{c^2}\right)(\gamma_3^2 - \gamma_1^2)D(KR)$$

$$\left. - 2(3\gamma_1^2 - \gamma_3^2)B + \frac{1}{c^2}D(KR)\right\}$$

$$\epsilon_{133} = \exp(-ivx_2)\frac{i}{4\rho R}\gamma_1\left\{2\left(\frac{1}{\alpha^2} - \frac{1}{c^2}\right)\gamma_3^2 D(QR)\right.$$

$$+ \left(\frac{1}{\beta^2} - \frac{1}{c^2}\right)(\gamma_1^2 - \gamma_3^2)D(KR)$$

$$\left. - 2(3\gamma_3^2 - \gamma_1^2)B + \frac{1}{c^2}D(KR)\right\}$$

$$\epsilon_{333} = \exp(-ivx_2)\frac{i}{4\rho R}\gamma_3\left\{2\left(\frac{1}{\alpha^2} - \frac{1}{c^2}\right)\gamma_3^2 D(QR)\right.$$

$$+ 2\left(\frac{1}{\beta^2} - \frac{1}{c^2}\right)\gamma_1^2 D(KR)$$

$$\left. + 2(3\gamma_1^2 - \gamma_3^2)B + \frac{2}{c^2}D(KR)\right\}$$

$$\epsilon_{113} = \exp(-ivx_2)\frac{i}{4\rho R}\gamma_3\left\{2\left(\frac{1}{\alpha^2} - \frac{1}{c^2}\right)\gamma_1^2 D(QR)\right.$$

$$\left. - 2\left(\frac{1}{\beta^2} - \frac{1}{c^2}\right)\gamma_1^2 D(KR) - 2(3\gamma_1^2 - \gamma_3^2)B\right\}$$

$$\epsilon_{331} = \exp(-ivx_2)\frac{i}{4\rho R}\gamma_1\left\{2\left(\frac{1}{\alpha^2} - \frac{1}{c^2}\right)\gamma_3^2 D(QR)\right.$$

$$\left. - 2\left(\frac{1}{\beta^2} - \frac{1}{c^2}\right)\gamma_3^2 D(KR) - 2(3\gamma_3^2 - \gamma_1^2)B\right\}$$

$$\epsilon_{121} = \exp(-ivx_2)\left[\frac{1}{4\rho cR}\{C(\gamma_3^2 - \gamma_1^2)\right.$$

$$\left. + \omega ER\gamma_1^2\} - \frac{\omega}{8\rho c}\{A - B(2\gamma_1^2 - 1)\}\right]$$

$$\epsilon_{233} = \exp\left(-ivx_2\right)\left[\frac{1}{4\rho cR}\{C(\gamma_1^2 - \gamma_3^2)\right.$$

$$\left. + \omega ER\gamma_3^2\} - \frac{\omega}{8\rho c}\{A - B(2\gamma_3^2 - 1)\}\right]$$

$$\epsilon_{112} = \exp\left(-ivx_2\right)\frac{1}{2\rho cR}\{C(\gamma_3^2 - \gamma_1^2) + \omega ER\gamma_1^2\}$$

$$\epsilon_{332} = \exp\left(-ivx_2\right)\frac{1}{2\rho cR}\{C(\gamma_1^2 - \gamma_3^2) + \omega ER\gamma_3^2\}$$

$$\epsilon_{122} = \exp\left(-ivx_2\right)\frac{i}{4\rho R}$$

$$\cdot\left\{\left(\frac{1}{\beta^2} - \frac{2}{c^2}\right)D(KR) + \frac{2}{c^2}D(QR)\right\}\gamma_1$$

$$\epsilon_{232} = \exp\left(-ivx_2\right)\frac{i}{4\rho R}$$

$$\cdot\left\{\left(\frac{1}{\beta^2} - \frac{2}{c^2}\right)D(KR) + \frac{2}{c^2}D(QR)\right\}\gamma_3$$

$$\epsilon_{123} = \exp\left(-ivx_2\right)\frac{\omega}{2\rho c}B\gamma_1\gamma_3$$

$$\epsilon_{231} = \exp\left(-ivx_2\right)\frac{\omega}{2\rho c}B\gamma_1\gamma_3$$

$$\epsilon_{132} = \exp\left(-ivx_2\right)\frac{\omega}{2\rho c}B\gamma_1\gamma_3$$

Laboratoire de Géophysique Interne et Tectonophysique
Université Joseph Fourier
F-38041 Grenoble Cedex
France
   (H.A.P., M.C.)

Instituto de Ingenieria
UNAM
Cd Universitaria
Coyoacán 04510, México D.F.
Mexico
   (F.J.S.)

Centro de Investigación Sísmica
Tlalpan 14200, México D.F.
Mexico
   (F.J.S.)